Journal of the Mechanics and Physics of Solids 61 (2013) 1585–1599

Contents lists available at SciVerse ScienceDirect

Journal of the Mechanics and Physics of Solids

journal homepage: www.elsevier.com/locate/jmps

Direct micromechanics derivation and DEM confirmation of the elastic moduli of isotropic particulate materials: Part II Particle rotation

J.A. Fleischmann [a,*], W.J. Drugan [b], M.E. Plesha [b]

[a] University of Wisconsin-Rock County, Department of Engineering, 2909 Kellogg Avenue, Janesville, WI 53546, United States
[b] University of Wisconsin-Madison, Department of Engineering Physics, 1500 Engineering Drive, Madison, WI 53706, United States

ARTICLE INFO

Article history:
Received 16 July 2012
Received in revised form
17 November 2012
Accepted 22 January 2013
Available online 4 February 2013

Keywords:
Micromechanics
Homogenization
Particulate material
Granular material
Discrete element method

ABSTRACT

In Part I, Fleischmann et al. (2013), we performed theoretical analyses of three cubic packings of uniform spheres (simple, body-centered, and face-centered) assuming no particle rotation, employed these results to derive the effective elastic moduli for a statistically isotropic particulate material, and assessed these results by performing numerical discrete element method (DEM) simulations with particle rotations prohibited. In this second part, we explore the effect that particle rotation has on the overall elastic moduli of a statistically isotropic particulate material. We do this both theoretically, by re-analyzing the elementary cells of the three cubic packings with particle rotation allowed, which leads to the introduction of an internal parameter to measure zero-energy rotations at the local level, and numerically via DEM simulations in which particle rotation is unrestrained. We find that the effects of particle rotation cannot be neglected. For unrestrained particle rotation, we find that the self-consistent homogenization assumption applied to the locally body-centered cubic packing incorporating particle rotation effects most accurately predicts the measured values of the overall elastic moduli obtained from the DEM simulations, in particular Poisson's ratio. Our new self-consistent results and theoretical modeling of particle rotation effects together lead to significantly better theoretical predictions of Poisson's ratio than all prior published results. Moreover, our results are based on a direct micromechanics analysis of specific geometrical packings of uniform spheres, in contrast to prior theoretical analyses based on hypotheses involving overall inter-particle contact distributions. Thus, our results permit a direct assessment of the reasons for the theory–experiment discrepancies noted in the literature with regard to previous theoretical derivations of the macroscopic elastic moduli for particulate materials, and our new theoretical results greatly narrow such discrepancies.

1. Introduction

In the first of this two-part series, Fleischmann et al. (2013), to which we refer simply as Part I in the sequel, we performed theoretical analyses of three cubic packings of uniform spheres (simple, body-centered, and face-centered) assuming no particle rotation. We used the resulting tensors of cubic elastic moduli **C** to obtain tensors of effective elastic

* Corresponding author. Tel.: +1 608 758 6565x713
E-mail address: jonathan.fleischmann@uwc.edu (J.A. Fleischmann).

0022-5096/$ - see front matter © 2013 Elsevier Ltd. All rights reserved.
http://dx.doi.org/10.1016/j.jmps.2013.01.009

moduli $\overline{\mathbf{C}}$ for a statistically isotropic particulate material with locally cubic packing structure, using the homogenization methods of Voigt (1928) (kinematic hypothesis), Reuss (1929) (static hypothesis), and Hershey (1954) and Kröner (1958) (self-consistent hypothesis). While the assumption of no particle rotation can be justified for certain regular cubic packings as the number of elementary cells becomes large (as we confirm herein), it cannot be justified in general for statistically isotropic assemblies that have only a *locally* cubic packing structure. In this second part of our two-part series, we re-analyze the three cubic packings with the effect of particle rotation included. We prove by several simple theoretical examples that particle rotation can produce zero-energy strains or mechanisms in a particulate material, and that they significantly alter the predicted value of Poisson's ratio for a particulate material in the elastic range. To account for the effect of particle rotation, we introduce a micromechanics-motivated internal parameter that leads to new theoretical predictions for the elastic moduli under all three homogenization assumptions.

After obtaining closed-form analytical expressions for the overall elastic moduli (bulk modulus and Poisson's ratio) of the particulate material in terms of the normal and tangential stiffnesses of the contacts between the particles in the material, we perform numerical simulations using the discrete element method (DEM) to measure the overall elastic moduli for specimens of randomly packed uniform spheres with constant normal and tangential contact stiffnesses (linear spring model), and we compare these results with the theoretical results obtained under the three homogenization assumptions for each of the three cubic packing geometries. In Part I, our DEM simulations were performed with particle rotation prohibited. In this second part, our DEM simulations are performed under identical conditions as in Part I, but with particle rotation unrestrained. The overall elastic moduli are again measured from the DEM simulations, and the results are compared both to those of the DEM simulations performed in Part I and to the theoretical results obtained in this second part, which include the effects of particle rotation. We show that our new theoretical results from the self-consistent hypothesis applied to the BCC packing including particle rotation agree most closely with DEM simulations in which particle rotation is unrestrained, and that these are significantly different from the results obtained in Part I when particle rotation was prohibited.

Our method of including the effects of mechanisms produced by particle rotation is in contrast to the work of other researchers, such as Chang et al. (1995) and Chang and Gao (1995), who include particle rotation only within the context of micro-polar or quasi-micro-polar continuum theory. The micro-polar or quasi-micro-polar continuum approach cannot capture the zero-energy strains or mechanisms produced by particle rotations, and therefore cannot accurately predict Poisson's ratio for an isotropic particulate material. We find that, when compared to the measured values of the overall elastic moduli obtained from DEM simulations on specimens of randomly packed uniform spheres, our analytical self-consistent results from the body-centered cubic packing that include the effect of particle rotation predict values of the elastic moduli, and in particular Poisson's ratio, that are significantly more accurate than those currently in the literature.

2. Overall elastic moduli for regular arrays of uniform spheres incorporating the effect of particle rotation

In Section 2 of Part I, we derived the three independent cubic elastic moduli C_1, C_2, and C_3 for three regular cubic packings of uniform spheres: face-centered cubic (FCC), simple cubic (SC), and body-centered cubic (BCC), under the assumption that no particle rotation occurred during deformation. These cubic elastic moduli were given in terms of the radius of the spheres R and the normal and tangential inter-particle contact stiffnesses K_n and K_t. They are repeated here for reference:

FCC, no particle rotation:

$$C_1 = \frac{1}{\sqrt{2}R}(K_n + K_t), \quad C_2 = \frac{1}{2\sqrt{2}R}(K_n - K_t), \quad C_3 = \frac{1}{2}C_1, \tag{1}$$

BCC, no particle rotation:

$$C_1 = \frac{1}{2\sqrt{3}R}(K_n + 2K_t), \quad C_2 = \frac{1}{2\sqrt{3}R}(K_n - K_t), \quad C_3 = \frac{1}{2}(C_1 + C_2), \tag{2}$$

SC, no particle rotation:

$$C_1 = \frac{1}{2R}K_n, \quad C_2 = 0, \quad C_3 = \frac{1}{4R}K_t, \tag{3}$$

The assumption that the particles (spheres) do not rotate turns out to be quite significant. Despite this fact, the assumption of no particle rotation can be justified for certain regular cubic arrays in the limit as the number of elementary cells becomes large, due to the symmetry of the inter-particle contacts; we provide explicit DEM verification of this later in this section. However, if a statistically isotropic particulate material has only *locally* cubic packing structure, then the assumption of no particle rotation can no longer be justified. What is even more problematic from the point of view of continuum modeling is that some of these particle rotations may be mechanisms. In other words, some quasi-static particle rotations may result in zero energy change in the system, but still cause plastic (irreversible) strain. This violates Drucker's postulate. Moreover, particle rotation at the local level may be involved in a global elastic strain of the particulate material, while, as Goddard (2008) shows, these particle rotations do not contribute to the quasi-static stress power. Mechanisms due to particle rotation can occur anywhere that there are local asymmetries in the distribution

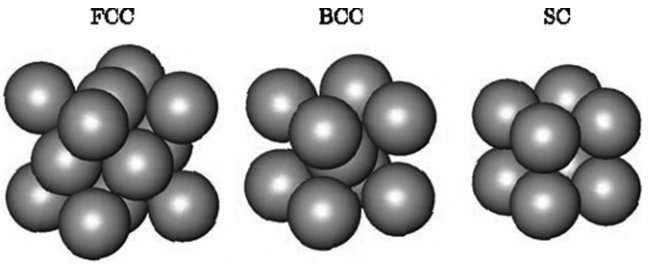

Fig. 1. Elementary cells of face-centered cubic (left), body-centered cubic (center), and simple cubic (right) regular arrays of uniform spheres.

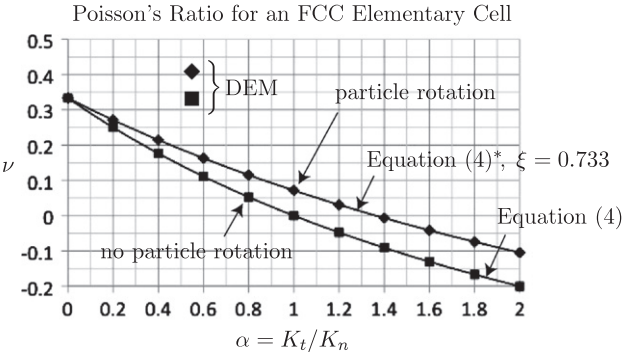

Fig. 2. Poisson's ratio ν as a function of $\alpha = K_t/K_n$ for a single elementary cell of an FCC array of uniform spheres. The data points represent values obtained by numerical simulations performed using the discrete element method (DEM) in which the particles were either allowed or not allowed to rotate. The theoretical curves are from Eqs. (4) and (4)* [which is Eq. (4) with α replaced by $\alpha^* = \xi\alpha$] with $\xi = 11/15 \approx 0.733$.

of inter-particle contacts. In the following subsections, we consider the effect of particle rotation in each of the three elementary cells shown in Fig. 1.

2.1. Face-centered cubic (FCC) array of uniform spheres

If we consider a single elementary cell of an FCC array of uniform spheres (Fig. 1, left), then for loading parallel to the principal axes, if the spheres are not allowed to rotate, Poisson's ratio is

$$\nu_{\mathrm{FCC}} = \frac{C_2}{C_1+C_2} = \frac{1-\alpha}{3+\alpha}, \tag{4}$$

with C_1 and C_2 given by Eq. (1) and $\alpha = K_t/K_n$. Fig. 2 plots Eq. (4), as well as measurements of Poisson's ratio ν as a function of α for the single elementary cell obtained from numerical simulations using the discrete element method. For one set of DEM simulations, the spheres were not allowed to rotate, while for the other set, rotation was unrestrained. In all of the DEM simulations, the lateral surfaces of the cell were constrained while an axial strain was applied quasi-statically along one of the principal axes (the z-axis), and Poisson's ratio was computed from the principal stress increments $d\sigma_x$, $d\sigma_y$, and $d\sigma_z$ according to Eq. (44) of Part I. No friction was present on the boundary of the elementary cell during the deformation. As Fig. 2 shows, when the spheres are not allowed to rotate, the DEM results for Poisson's ratio are in perfect agreement with the theoretical predictions of Eq. (4). When the spheres are allowed to rotate, however, the DEM results for Poisson's ratio no longer agree with the theoretical predictions of Eq. (4), but are consistently (and significantly) higher. Note that we were able to verify that there was *no inter-particle slip* in all of the DEM simulations referred to in Fig. 2.

It is not difficult to theoretically determine the effect of particle rotation on the cubic elastic moduli of a single FCC elementary cell with no friction between the spheres and the boundary of the cell. First, we note that Eq. (1) can be re-derived for the case of no particle rotation by considering a single FCC elementary cell subjected to a state of pure uniaxial strain $\epsilon_{11} = -\delta_{11}/(\sqrt{2}D)$ (with $\epsilon_{22} = \epsilon_{33} = 0$). It can be shown by an analysis of the inter-particle normal and tangential contact forces within the FCC cell that the forces normal to the cell faces are $F_{11} = -2(K_n+K_t)\delta_{11}$ and $F_{22} = F_{33} = -(K_n-K_t)\delta_{11}$, where contributions from inter-particle contacts on the faces and interior of the cell have been included, and where, since the "material" cube is measured only to the centers of the outer spheres, the normal and tangential stiffnesses of the contacts on the faces contribute half of their full values. From these expressions for C_1 and C_2 in terms of K_n and K_t given in Eq. (1) can be derived in a straightforward way, since $\sigma_{11} = F_{11}/(2D^2) = C_1\epsilon_{11}$ and $\sigma_{22} = \sigma_{33} = F_{22}/(2D^2) = F_{33}/(2D^2) = C_2\epsilon_{11}$. Similarly, the expression for C_3 in terms of K_n and K_t given in Eq. (1) can be derived by considering a single FCC elementary cell subjected to a state of pure shear.

If a single FCC elementary cell in which particle rotation is *unrestrained* is subjected to a state of pure uniaxial strain along one of its principal axes, then due to the symmetry of the loading, only the spheres at the eight corners of the cell will experience rotation. Note that in the FCC packing, each corner sphere is in contact with three face-centered spheres: two on faces parallel to the axis of deformation and one on a face normal to the axis of deformation. If each corner sphere remains in contact with all three face-centered spheres throughout the deformation, then an analysis of the stiffness matrix for the FCC elementary cell with rotational degrees of freedom leads to $F_{11}=-2(K_n+\xi K_t)\delta_{11}$ and $F_{22}=F_{33}=-(K_n-\xi K_t)\delta_{11}$ with $\xi=11/15$. This analysis is given in detail in Appendix A. It follows that the cubic elastic moduli for the FCC elementary cell with unrestrained particle rotation are

$$C_1=\frac{1}{\sqrt{2}R}(K_n+\xi K_t),\quad C_2=\frac{1}{2\sqrt{2}R}(K_n-\xi K_t),\quad C_3=\frac{1}{2}C_1, \tag{5}$$

with $\xi=11/15\approx 0.733$.

If the deformation in the single FCC elementary cell we have just described is sufficiently large, then infinitesimal gaps will form between the corner spheres and the face-centered spheres on faces normal to the axis of deformation. In this case, if particle rotation is unrestrained and no tangential force is applied to the boundaries of the cell, it can be shown by a similar analysis that the cubic elastic moduli for the FCC elementary cell are again given by Eq. (5), but now with $\xi=0.5$. If particle rotation is prohibited, then gaps on the faces normal to the deformation may still form, but they do not affect the cubic elastic moduli (i.e., $\xi=1$).

Our theoretical analysis is confirmed by the DEM simulations described at the beginning of this section. If we substitute the expressions for C_1 and C_2 given by Eq. (5) into Eq. (4), and call the resulting expression Eq. (4)* where $\alpha^*=\xi\alpha$ replaces α, then the $\nu(\alpha)$ curve predicted by Eq. (4)* with $\xi=0.733$ agrees perfectly with the curve that was obtained numerically by DEM simulations in which particle rotation was unrestrained, as shown in Fig. 2.

We commented earlier that the assumption of no particle rotation *is* valid for certain regular cubic arrays in the limit as the number of elementary cells becomes large. This is in fact true for the regular FCC array even when the number of elementary cells is only moderately large. We have confirmed this by DEM simulations on $2\times2\times2$, $3\times3\times3$, and $7\times7\times7$ arrays of FCC elementary cells, containing totals of 63, 172, and 1688 uniform spheres, respectively. The results are shown in Fig. 3. For a $7\times7\times7$ FCC array, the data points obtained from DEM simulations in which particle rotation was *unrestrained* match those obtained from a single FCC elementary cell in which particle rotation was prohibited, which is predicted by Eq. (4) or by Eq. (4)* with $\xi=1$, as shown in Fig. 3; this is the minimum array size for which this match occurs.

2.2. Body-centered cubic (BCC) array of uniform spheres

If we consider a single elementary cell of a BCC array of uniform spheres (Fig. 1, center), then for loading parallel to the principal axes, if the spheres are not allowed to rotate, Poisson's ratio is

$$\nu_{BCC}=\frac{C_2}{C_1+C_2}=\frac{1-\alpha}{2+\alpha}, \tag{6}$$

with C_1 and C_2 given by Eq. (2). It is quite easy to show theoretically that if particle rotation is allowed for a single BCC elementary cell loaded parallel to the principal axes with no friction on the boundary of the cell, then $\nu_{BCC}=0.5$ regardless of α. This is confirmed by DEM simulations analogous to those performed on the single FCC elementary cell considered in Section 2.1. Fig. 4 plots Eq. (6), as well as measurements of Poisson's ratio ν as a function of α for the single elementary cell obtained from numerical simulations using the discrete element method. For one set of DEM simulations, the spheres were not allowed to rotate, while for the other set, rotation was unrestrained. No friction was present on the boundary of the

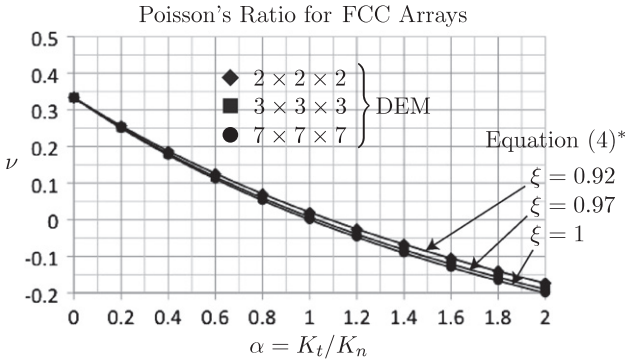

Fig. 3. Poisson's ratio ν as a function of $\alpha=K_t/K_n$ for $2\times2\times2$, $3\times3\times3$, and $7\times7\times7$ arrays of FCC elementary cells, containing totals of 63, 172, and 1688 uniform spheres, respectively. The data points represent values obtained by numerical simulations performed using the discrete element method (DEM) in which particle rotation was unrestrained. The theoretical curves are from Eq. (4)* [which is Eq. (4) with α replaced by $\alpha^*=\xi\alpha$] with $\xi=0.92$, $\xi=0.97$, and $\xi=1$. The $7\times7\times7$ array is the minimum size for which $\xi=1$.

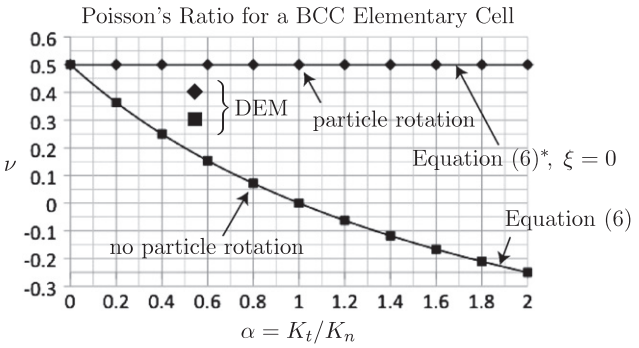

Fig. 4. Poisson's ratio ν as a function of $\alpha = K_t/K_n$ for a single elementary cell of a BCC array of uniform spheres. The data points represent values obtained by numerical simulations performed using the discrete element method (DEM) in which the particles were either allowed or not allowed to rotate. The theoretical curves are from Eqs. (6) and (6)* [which is Eq. (6) with α replaced by $\alpha^* = \xi\alpha$] with $\xi = 0$.

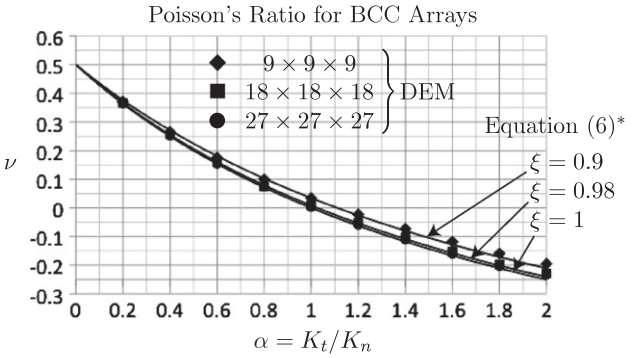

Fig. 5. Poisson's ratio ν as a function of $\alpha = K_t/K_n$ for $9 \times 9 \times 9$, $18 \times 18 \times 18$, and $27 \times 27 \times 27$ arrays of BCC elementary cells, containing totals of 1729, 12 691, and 41 635 uniform spheres, respectively. The data points represent values obtained by numerical simulations performed using the discrete element method (DEM) in which particle rotation was unrestrained. The theoretical curves are from Eq. (6)* [which is Eq. (6) with α replaced by $\alpha^* = \xi\alpha$] with $\xi = 0.9$, $\xi = 0.98$, and $\xi = 1$. The $27 \times 27 \times 27$ array is the minimum size for which $\xi \approx 1$.

elementary cell during the deformation. As Fig. 4 shows, when the spheres are not allowed to rotate, the DEM results for Poisson's ratio are in perfect agreement with the theoretical predictions of Eq. (6). When the spheres are allowed to rotate, however, the DEM results for Poisson's ratio no longer agree with the theoretical predictions of Eq. (6), but are consistently (and significantly) higher. Note that we were able to verify that there was *no inter-particle slip* in either of the DEM simulations referred to in Fig. 4.

Indeed, for any sort of deformation, if the spheres in a BCC elementary cell are free to rotate and there is no tangential force applied to the boundaries, there will be no inter-particle tangential displacement regardless of K_t. This follows immediately from moment equilibrium applied to the eight spheres on the boundaries of the cell. Thus, the effect of particle rotation for a single BCC elementary cell with particle rotation unrestrained is equivalent to the inter-particle tangential stiffness being zero. In analogy to the cases of the FCC and SC elementary cells, we can write the modified cubic elastic moduli for a single BCC elementary cell incorporating particle rotation as

$$C_1 = \frac{1}{2\sqrt{3}R}(K_n + 2\xi K_t), \quad C_2 = \frac{1}{2\sqrt{3}R}(K_n - \xi K_t), \quad C_3 = \frac{1}{2}(C_1 + C_2), \tag{7}$$

with $\xi = 0$.

Our theoretical analysis is confirmed by the DEM simulations described at the beginning of this section. If we substitute the expressions for C_1 and C_2 given by Eq. (7) into Eq. (6), and call the resulting expression Eq. (6)* where $\alpha^* = \xi\alpha$ replaces α, then the $\nu(\alpha)$ curve predicted by Eq. (6)* with $\xi = 0$ agrees exactly with the curve that was obtained numerically by DEM simulations in which particle rotation was unrestrained, as shown in Fig. 4. It is noteworthy that, due to geometric nonlinearities, if the pre-compression on the single BCC elementary cell in the DEM simulations results in an initial overlap of the spheres of $0.01D$, where D is the sphere diameter, then the DEM results for Poisson's ratio are actually $\nu = 0.508$. However, if the pre-compression on the single BCC elementary cell is reduced so that the initial overlap of the spheres is $0.001D$, then the DEM result for Poisson's ratio becomes $\nu = 0.5008$, and this result can be brought arbitrarily close to the theoretical result of $\nu = 0.5$ by further reducing the initial overlap of the spheres.

Unlike the case of the FCC elementary cells, however, it takes a significant number of BCC elementary cells to restrain particle rotation. Fig. 5 shows the results of DEM simulations on $9 \times 9 \times 9$, $18 \times 18 \times 18$, and $27 \times 27 \times 27$ arrays of BCC

elementary cells, containing totals of 1729, 12 691, and 41 635 uniform spheres, respectively. For a $27 \times 27 \times 27$ BCC array, the data points obtained from DEM simulations in which particle rotation was unrestrained match approximately those obtained from a single BCC elementary cell in which particle rotation was prohibited (the match is good for $\alpha \leq 1.0$, but it diverges slightly for $\alpha > 1.0$), which is predicted by Eq. (6) or by Eq. (6)* with $\xi = 1$, as shown in Fig. 5; this is the minimum array size for which this approximate match occurs.

2.3. Simple cubic (SC) array of uniform spheres

A single elementary cell of a SC array of uniform spheres (Fig. 1, right) shows no Poisson effect when loaded parallel to the principal axes (because $C_2 = 0$). However, particle rotation can affect the shear behavior of a single SC elementary cell when asymmetries exist in the distribution of inter-particle contacts, which result in shearing mechanisms. To illustrate this point with a simple example, consider an elementary cell of a simple cubic array of uniform spheres subjected to pure shear for which particle rotation *is allowed* to occur, as shown in Fig. 6. If all of the inter-particle contacts in the SC elementary cell shown in Fig. 6 are active, then a simple calculation shows that the shear strain is $2\epsilon_{xy} = \Delta/2R$, and the shear stress is $\sigma_{xy} = 4K_t\delta_t/(4R)^2$, where $\delta_t = \Delta - 2R\theta$ and R is the radius of the spheres. Moment balance at the particle level requires that $K_t\delta_t = K_t 2R\theta$, from which it follows that $\Delta = 2\delta_t$. Thus, it follows in this case that $C_3 = \sigma_{xy}/(2\epsilon_{xy}) = K_t/(4R)$, which is the same as the value reported for the SC elementary cell in Eq. (3) obtained assuming *no* particle rotation. Note that in this case the distribution of inter-particle contacts in Fig. 6 is symmetric.

Next consider the same SC elementary cell subjected to pure shear shown in Fig. 6, but this time with a single infinitesimal gap introduced between the two visible spheres at the bottom of the cell, so that there is no resistance to relative rotation at what would otherwise have been the contact point between those two spheres in the y–z plane. It follows that, while the shear strain is the same as it was in the preceding paragraph when all of the inter-particle contacts were active, and moment balance at the particle level still requires that $K_t\delta_t = K_t 2R\theta$ (in the absence of moments at the inter-particle contacts), the shear stress now becomes $\sigma_{xy} = 2K_t\delta_t/(4R)^2$, from which it follows that $C_3 = 0.5K_t/(4R)$, which is *half* of the value reported for the SC elementary cell in Eq. (3) assuming no particle rotation. Note that in this case the distribution of inter-particle contacts in Fig. 6 is no longer symmetric.

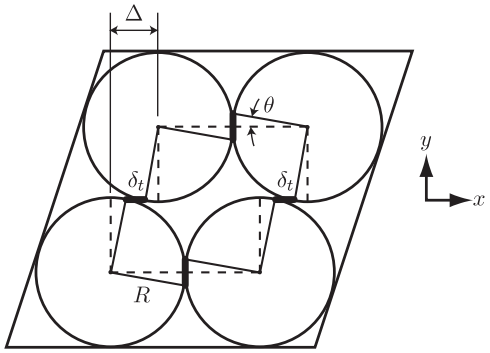

Fig. 6. An elementary cell of an SC array of uniform spheres subjected to pure shear. If all inter-particle contacts are active, then $C_3 = K_t/(4R)$, which is the same as when no particle rotation is allowed, and corresponds to $\xi = 1.0$ in Eq. (8). However, if a single infinitesimal gap is introduced between the two visible spheres at the bottom of the cell so that one inter-particle contact in the y–z plane is lost, then $C_3 = 0.5K_t/(4R)$, which corresponds to $\xi = 0.5$ in Eq. (8).

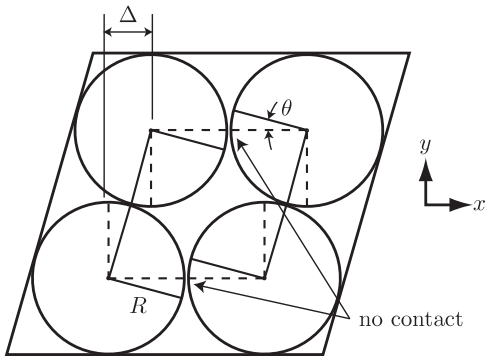

Fig. 7. An elementary cell of an SC array of uniform spheres subjected to pure shear, with no inter-particle contacts in the y–z plane. For this arrangement $C_3 = 0$, which corresponds to $\xi = 0$ in Eq. (8).

Finally, consider the same SC elementary cell subjected to pure shear shown in Fig. 7, in which an infinitesimal gap exists between all pairs of particles having their contact plane with unit normal in the x-direction. This arrangement provides no resistance to shear stress, and so $C_3 = 0$.

These simple examples suggest that if we consider the possibility of zero-energy shearing mechanisms due to particle rotation and asymmetry in the distribution of inter-particle contacts, the cubic elastic moduli for a single SC elementary cell become

$$C_1 = \frac{1}{2R}K_n, \quad C_2 = 0, \quad C_3 = \frac{1}{4R}\xi K_t, \tag{8}$$

where $0 \le \xi \le 1$ is an internal parameter measuring the presence of shearing mechanisms due to particle rotation and asymmetries in the distribution of inter-particle contacts. In the preceding three examples, we found by direct analysis that $\xi = 1.0$, $\xi = 0.5$, or $\xi = 0$, respectively, depending on the number of inter-particle contacts providing resistance to shear deformation. Note that in all three of these examples the resistance of the elementary cell to normal stress (and hence the value of C_1) is the same.

3. Isotropic effective elastic moduli incorporating the effect of particle rotation

In Section 3 of Part I, we derived relations between the overall elastic moduli $\overline{\kappa}$ and $\overline{\nu}$ of a statistically isotropic particulate material on the macroscale, and the normal and tangential inter-particle contact stiffnesses K_n and K_t (and $\alpha = K_t/K_n$) and the average number of inter-particle contacts per unit volume β on the microscale, for all three local cubic packings under the Voigt, Reuss, and self-consistent hypotheses. If Eqs. (5), (7) and (8) are used for the cubic elastic moduli instead of Eqs. (1)–(3), then the only change in the relations obtained in Section 3 of Part I is that K_t is replaced by an "effective" $K_t^* = \xi K_t$, and α is replaced by an "effective" $\alpha^* = \xi\alpha = K_t^*/K_n$, where $0 \le \xi \le 1$ is an internal parameter measuring the presence of shearing mechanisms due to particle rotation and asymmetries in the distribution of inter-particle contacts. Note that K_n remains unchanged. If $\xi = 0$ then all inter-particle contacts contain shearing mechanisms, and K_t becomes zero. If $\xi = 1$ then there are no shearing mechanisms, and K_t is unaltered.

Thus, we obtain the following relations between the normal and tangential inter-particle contact stiffnesses K_n and K_t (and $\alpha = K_t/K_n$) and the parameter β on the microscale, and the overall elastic moduli $\overline{\kappa}$ and $\overline{\nu}$ of the particulate material on the macroscale, under the Voigt, Reuss, and self-consistent hypotheses for the locally FCC, BCC, and SC packings:

$$\text{Voigt, Reuss, self}-\text{consistent : FCC, BCC, SC :} \quad \overline{\kappa} = \frac{\beta D^2}{9}K_n, \tag{9}$$

$$\text{Voigt : FCC, BCC, SC :} \quad \overline{\nu} = \frac{1-\alpha^*}{4+\alpha^*}, \tag{10}$$

$$\text{Reuss : FCC :} \quad \overline{\nu} = \frac{3+2\alpha^*-5\alpha^{*2}}{11+24\alpha^*+5\alpha^{*2}}, \tag{11}$$

$$\text{Reuss : BCC :} \quad \overline{\nu} = \frac{4+\alpha^*-5\alpha^{*2}}{8+32\alpha^*+5\alpha^{*2}}, \tag{12}$$

$$\text{Reuss : SC :} \quad \overline{\nu} = \frac{1-\alpha^*}{2+3\alpha^*}, \tag{13}$$

$$\text{self-consistent : FCC :} \quad \alpha^* = \frac{2+5\overline{\nu}-5\overline{\nu}^2-8\overline{\nu}^3-\sqrt{36-144\overline{\nu}+88\overline{\nu}^2+280\overline{\nu}^3-291\overline{\nu}^4-134\overline{\nu}^5+169\overline{\nu}^6}}{-4-3\overline{\nu}+6\overline{\nu}^2+5\overline{\nu}^3}, \tag{14}$$

$$\text{self-consistent : BCC :} \quad \alpha^* = \frac{11+30\overline{\nu}-27\overline{\nu}^2-46\overline{\nu}^3-3\sqrt{81-228\overline{\nu}+202\overline{\nu}^2+352\overline{\nu}^3-735\overline{\nu}^4-92\overline{\nu}^5+484\overline{\nu}^6}}{4(-4-3\overline{\nu}+6\overline{\nu}^2+5\overline{\nu}^3)}, \tag{15}$$

$$\text{self-consistent : SC :} \quad \alpha^* = \frac{(1-2\overline{\nu})^2(3-\overline{\nu})}{(1+\overline{\nu})^2(3-4\overline{\nu})}, \tag{16}$$

where $\alpha^* = \xi\alpha = \xi K_t/K_n$, and where α^* is written in terms of $\overline{\nu}$ in the self-consistent case only because the expressions are far more concise than the corresponding expressions for $\overline{\nu}$ in terms of α^*.

In Section 2.1, for a single FCC cell with unrestrained particle rotation and no tangential force applied to the boundaries, we found by direct analysis that $\xi = 0.733$ or $\xi = 0.5$, depending on whether or not certain infinitesimal inter-particle gaps exist. We also found by DEM simulations on $2 \times 2 \times 2$, $3 \times 3 \times 3$, and $7 \times 7 \times 7$ arrays of FCC cells with unrestrained particle rotation that $\xi = 0.92$, $\xi = 0.97$, and $\xi = 1$, respectively, as shown in Fig. 3. In Section 2.2, for a single BCC cell with unrestrained particle rotation and no tangential force applied to the boundaries, we found by direct analysis that $\xi = 0$. We also found by DEM simulations on $9 \times 9 \times 9$, $18 \times 18 \times 18$, and $27 \times 27 \times 27$ arrays of BCC cells with unrestrained particle rotation that $\xi = 0.9$, $\xi = 0.98$, and $\xi = 1$, respectively, as shown in Fig. 5. For both the FCC and BCC arrays, the *minimum* number of cells was found that effectively restrained particle rotation (i.e., resulted in $\xi = 1$), and this is the number that

was reported. Note that significantly more cells were required to restrain particle rotation in the BCC array than were required in the FCC array. In Section 2.3, for a single SC cell subjected to pure shear with unrestrained particle rotation, we found by direct analysis that $\xi = 1.0$, $\xi = 0.5$, or $\xi = 0$, depending on the number of infinitesimal inter-particle gaps introduced. Note that if $\xi = 0$ then Eqs. (12), (13) and (16) predict that $\overline{\nu} = 0.5$ for all values of α. This suggests that in the presence of sufficiently many shearing mechanisms, the particulate material acts effectively as a fluid, with no resistance to shear stress. The case of $\xi = 0$ is illustrated by the SC elementary cell considered in Fig. 7, and by the single BCC elementary cell with unrestrained particle rotation. It should be noted, however, that these two illustrative cases are not isotropic. For further discussion of the arrangement shown in Fig. 7, see Bardet and Vardoulakis (2001) and Kruyt (2003).

While it is clear that (infinitely) many rotational mechanisms exist in a single BCC elementary cell when no tangential force is applied to the spheres in contact with the cell boundary, for such mechanisms to exist in a *statistically isotropic aggregate* of BCC elementary cells, it would be necessary for some kind of local asymmetry to exist in the inter-particle contact distribution. Such local asymmetry could be caused by a series of aligned BCC elementary cells. Note that a diagonal alignment of BCC cells would result in what is called a "force-chain" in the geomechanics literature. The existence of force-chains in particulate materials is well known, as noted by Mitchell and Soga (2005). Force-chains, sometimes called strong force networks, refer to isolated paths of high inter-particle contact forces within a particulate material under load. The areas outside of these force-chains, sometimes called weak clusters, experience much smaller inter-particle contact forces. Many researchers, such as Cundall and Strack (1979) and Oda (1997), have observed that during plastic shear, particles within force-chains do not slide, but rather the columns of particles within the force-chains buckle. In an elastic context, the buckling of local force-chains in a particulate material (which implies the existence of local mechanisms due to particle rotation) would result in an increase in Poisson's ratio when compared to a particulate material without such mechanisms, as predicted by Eqs. (10)–(16) when $\xi < 1$.

It is intriguing to consider the relationship between the parameter ξ and other internal geometrical parameters of a (statistically isotropic) particulate material, such as the average number of contacts per unit volume β, or the average coordination number $\overline{n}_c$, which is related to β (see,e.g., Nemat-Nasser, 2004). Note, however, that in Eq. (9) the value of β is unaffected by ξ. This is because the particle rotations and infinitesimal gaps considered in the preceding subsections did not affect the *normal* component of the inter-particle contact forces, and so did not change the bulk modulus $\overline{\kappa}$. Hence, the average number of contacts per unit volume β should still include the "missing" contacts that in some of these examples gave rise to $\xi < 1$. Thus, the internal parameter ξ cannot depend exclusively on either β or $\overline{n}_c$. Rather, we hypothesize that the internal parameter ξ for an overall isotropic particulate material is related to *local asymmetry* in the inter-particle contact force distribution. Finding a relationship between the internal parameter ξ and a quantifiable measure of asymmetry in the inter-particle contact force distribution of a particulate material at the local level, which must involve the fabric tensor of the particulate material (e.g., Durán et al., 2010), is a subject of continuing research.

Recent work in determining the effective isotropic elastic moduli for a particulate (or granular) material based on micromechanics, with an attempt to include the effect of particle rotation, has been performed by Suiker and de Borst (2005). They rederive the relations expressed by the Voigt equation (10) with $\xi = 1$ (but without the internal parameter), along with additional relations for higher order elastic constants corresponding to several strain-gradient micro-polar continuum models. Then they compare the predictions of these models with the wave propagation characteristics of a two-dimensional discrete hexagonal lattice. Their analysis follows that of Chang and Liao (1990) and Chang and Gao (1995) in assuming that discrete particle rotations can be approximated by a continuous particle rotation field, similar to the strain field of classical continuum theory. This particle rotation field is then represented by a Taylor expansion, which can be truncated at whatever order is desired for the strain-gradient continuum model. This approach is problematic in that it cannot capture the zero-energy strains or mechanisms due to particle rotation at the microscale. Both the simple example of this section and the DEM results of Section 4 demonstrate that mechanisms due to particle rotation can and do exist in a random assembly of spherical particles, and these mechanisms affect the elastic properties of the material (specifically Poisson's ratio), despite the fact that they do not contribute to the quasi-static stress power (Goddard, 2008). As will be shown in the following section, none of these prior theoretical models incorporating particle rotation can come close to matching our DEM simulations for precisely these reasons, whereas the theoretical models derived here can.

4. Validation by the discrete element method

To test the analytical results of Section 3, we performed numerical simulations using the discrete element method (DEM) to measure the macroscopic elastic moduli for randomly packed aggregates of uniform spheres having constant normal and tangential contact stiffnesses K_n and K_t, respectively. We report the results that we have obtained from six DEM specimens. Specimens 1, 2, and 3 each contained 3430 randomly packed uniform spheres, and Specimens 4, 5, and 6 each contained 29 660 randomly packed uniform spheres. The specimens are shown in Fig. 7 of Part I.

We performed the DEM simulations using the open source code LAMMPS, described in Part I. The setup procedure and initial geometries of the six DEM specimens used in this part of our two-part series are identical to those of the six DEM specimens used in Part I. For a discussion of the initial packing geometries, including the average number of contacts per unit volume and the radial distribution functions for the specimens, see Section 5 and Fig. 9 of Part I.

To measure Poisson's ratio $\overline{\nu}$ for each specimen, we followed the procedure described by the paragraph including Eq. (44) in Part I. To explore the effect of particle rotation in the DEM simulations of this second part of our two-part series, the spheres were allowed full three-dimensional translational and rotational freedom of motion. The results are shown in Fig. 8. Data points for both of the measured values of Poisson's ratio $\overline{\nu}_1$ and $\overline{\nu}_2$ given by Eq. (44) of Part I are included in all of the figures as solid squares and solid diamonds. The difference between these data points provides a rough measure of the anisotropy of the specimens, at least in the directions normal to the specimen boundaries. Note that in most of the figures, these data points lie roughly on top of one another.

Fig. 8 also shows the Voigt (10), Reuss (13), and self-consistent (15), (16) curves, with $\xi = \{0.75,0.6,0.55,0.85,0.8,0.75\}$ for Specimens 1–6, respectively, where the values of the internal parameter ξ were chosen to fit the DEM data points. Also shown in Fig. 8 by dotted lines are all of the same curves with $\xi = 1$, which correspond to the curves shown in Fig. 8 of Part I. Note that when the rotation of the spheres is not restrained, the value of Poisson's ratio in all six specimens is strictly and significantly greater than zero when $\alpha = 1.0$ ($K_t = K_n$). This is in disagreement with the results of Section 3 in Part I, which do not account for the effect of particle rotation, as well as the results of Chang et al. (1995) for both an isotropic and a general anisotropic particulate material (not necessarily having a locally cubic packing structure) under both the kinematic and static hypotheses, all of which predict $\overline{\nu} = 0$ when $\alpha = 1.0$. This phenomenon *is* captured, however, by Eqs. (10), (13), (15) and (16), with $\xi < 1.0$.

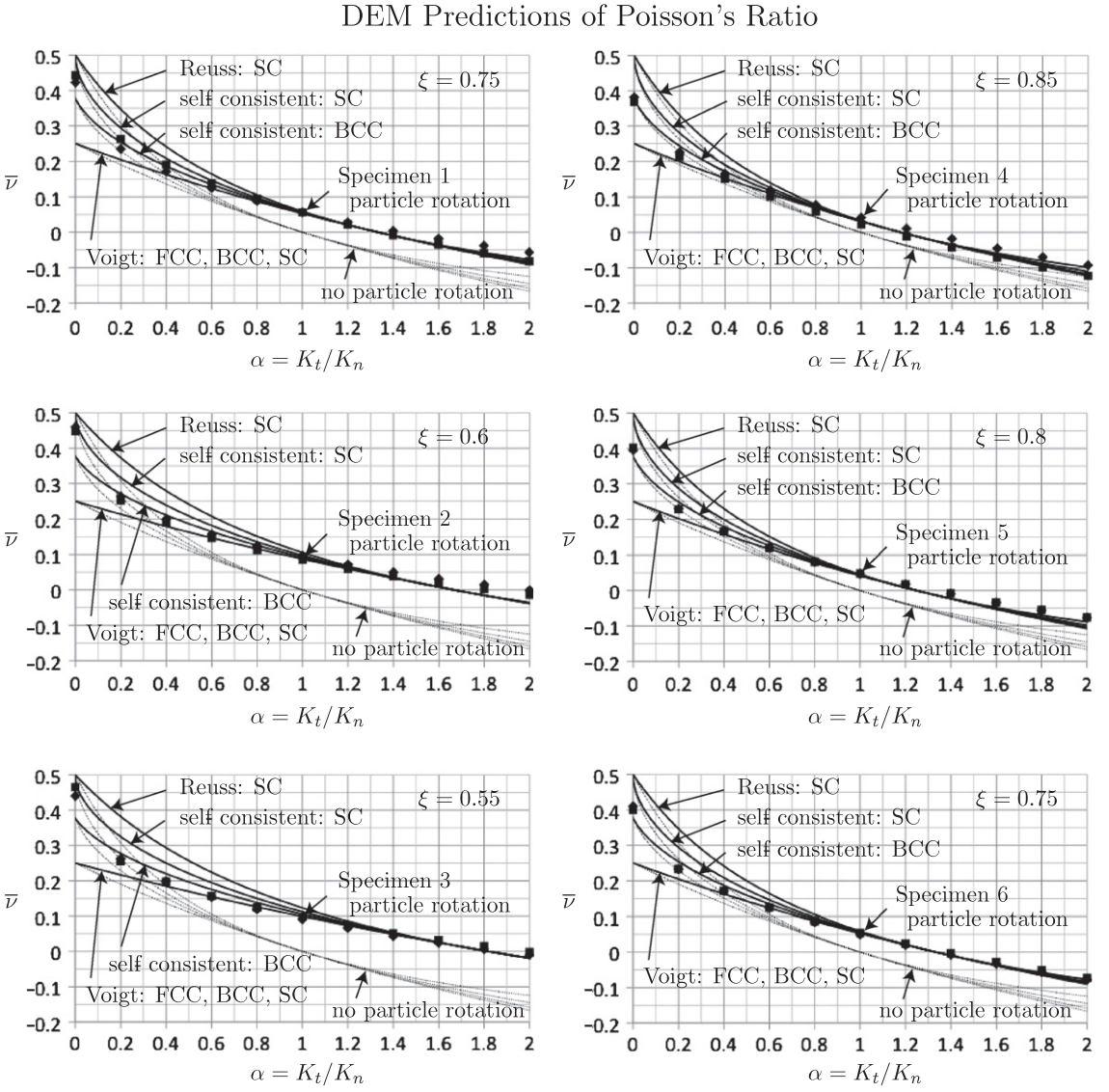

Fig. 8. Macroscopic Poisson's ratio $\overline{\nu}$ versus $\alpha = K_t/K_n$ obtained from DEM simulations on six specimens of randomly packed uniform spheres with constant normal and tangential contact stiffnesses K_n and K_t, in which the spheres were allowed to rotate. Also shown are the theoretical curves given by Eqs. (10) (Voigt: FCC, BCC, SC), (13) (Reuss: SC), (15) and (16) (self-consistent: BCC and SC, respectively), with $\xi = \{0.75,0.6,0.55,0.85,0.8,0.75\}$ for Specimens 1-6 respectively. Observe that the analytical self-consistent homogenization result for the local BCC packing, Eq. (15), agrees most closely with the DEM simulations.

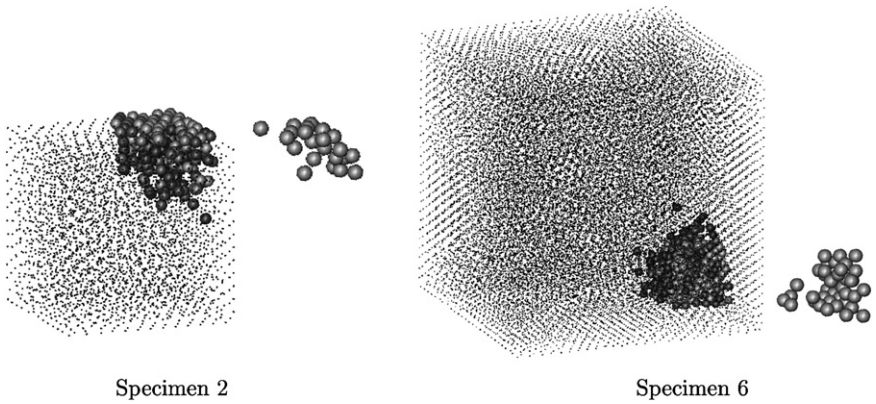

Fig. 9. Rotational mechanisms in DEM Specimens 2 and 6. The particles represented as spheres in each specimen experienced rotations in excess of two times the rms-average particle rotation in the specimen. The magnified spheres next to Specimens 2 and 6 represent particles that experienced rotations in excess of five and 10 times the rms-average particle rotation, respectively.

In particular, the relationship between Poisson's ratio $\overline{\nu}$ and $\alpha = K_t/K_n$ that is given by Eq. (15), the self-consistent result for the local BCC packing, with $\xi = \{0.75,0.6,0.55,0.85,0.8,0.75\}$ for Specimens 1–6, respectively, agrees with the values obtained from the DEM simulations better than any of the other theoretical predictions we have considered thus far.

We also monitored friction work between the spheres throughout the DEM simulations, and we verified that *there was no inter-particle slip* during the DEM simulations, regardless of whether or not particle rotation was allowed (i.e., friction work was zero). Thus, inter-particle slip, and consequently plastic deformation, was not involved in the discrepancy between the values of Poisson's ratio predicted by the Voigt (10), Reuss (13), and self-consistent (15) and (16) equations, with $\xi = 1$, which also correspond to the equations of Section 3 in Part I, and the values that were measured from the DEM simulations when particle rotation was allowed. As noted above, this discrepancy increased as α increased, but was remedied when the Voigt, Reuss, and self-consistent equations were used with $\xi = \{0.75,0.6,0.55,0.85,0.8,0.75\}$ for Specimens 1–6, respectively. Note that, because Chang et al. (1995) predict $\overline{\nu} = 0$ when $\alpha = 1.0$ not only for a statistically isotropic particulate material, but also for a general anisotropic particulate material, their theoretical predictions cannot be reconciled with our DEM results when particle rotation is involved. We postulate that the internal parameter ξ measures zero-energy rotations or mechanisms in the particulate material at the local level (as it was directly shown to do in the explicit cases analyzed in Sections 2.1–2.2), which exist even when the particulate material is statistically isotropic and when no inter-particle slip occurs, and which, as we discussed at the end of Section 3, are not accounted for in the quasi-micro-polar and micro-polar theories of Chang et al. (1995), Chang and Gao (1995), Suiker and de Borst (2005), and others.

Our postulation of the existence of zero-energy rotations or mechanisms in a statistically isotropic particulate material (which we have directly confirmed: see the last two paragraphs of this section) is similar to the postulation made by Jenkins et al. (2005), who, following earlier work by Jenkins et al. (1989), have used DEM simulations to show that *local deviations* in strain from the average (macroscopic) strain in a particulate material can lead to *large* discrepancies between the theoretically predicted values of the macroscopic shear modulus (or Poisson's ratio) for the particulate material and the numerically measured values. They argue that this local deviation is due to strain "relaxation" between particle pairs, which is similar to our argument for local strain "mechanisms" due to particle rotation. Jenkins et al. (2005) show that this local strain relaxation can decrease the theoretical prediction of the effective shear modulus obtained from Eq. (24) of Part I, or Eqs. (9) and (10) with $\xi = 1$ (where the shear modulus is obtained in terms of the bulk modulus $\overline{\kappa}$ and Poisson's ratio $\overline{\nu}$), by up to 70%. In contrast, they found that the bulk modulus $\overline{\kappa}$ is relatively insensitive to local strain variation. This is in perfect agreement with our observations in Section 3 and in this section regarding Poisson's ratio. The DEM specimens used by Jenkins et al. (2005) consist of 10 000 randomly packed spheres of two different radii in equal numbers.

We have confirmed the existence of rotational mechanisms within our DEM specimens by monitoring the angular velocities of individual particles throughout the DEM simulations described in this section. We found that particles in some of the specimens experienced angular velocities in excess of 10 *times* the average angular velocity of the particles in those specimens during a simulation. This can be quantified by the ratio $\langle \Omega \rangle_{\max}/\langle \Omega \rangle_{\text{avg}}$, where Ω is the magnitude of the angular velocity of an individual particle in a specimen, the angled brackets $\langle\ \rangle$ denote root-mean-square time average over the course of a simulation, and the subscripts "max" and "avg" denote maximum and rms-average values over all particles in the specimen. We computed this ratio for each specimen during the simulation with $\alpha = 1.0$, and the resulting values were $\langle \Omega \rangle_{\max}/\langle \Omega \rangle_{\text{avg}} = \{10.3,8.37,9.31,32.9,70.0,36.4\}$ for Specimens 1–6, respectively.

Fig. 9 shows clusters of particles in Specimens 2 and 6 that experienced angular velocities in excess of two times the rms-average particle angular velocity at a particular time during the DEM simulations with $\alpha = 1.0$. The particles with $\Omega > 2\Omega_{\text{avg}}$ are shown as spheres in Fig. 9, while the other particles (i.e., with $\Omega \le 2\Omega_{\text{avg}}$) are shown as dots. The spheres are shaded according to the magnitude of their angular velocities. Particles with $\Omega > 5\Omega_{\text{avg}}$ and $\Omega > 10\Omega_{\text{avg}}$ are magnified and shown next to Specimens 2 and 6, respectively. Fig. 9, together with the measured values of $\langle \Omega \rangle_{\max}/\langle \Omega \rangle_{\text{avg}}$ for all of

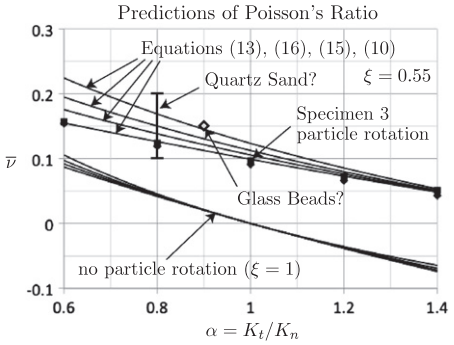

Fig. 10. Macroscopic Poisson's ratio $\overline{\nu}$ for $\alpha = K_t/K_n$ bounded by $2/3 \le \alpha \le 4/3$, which is the range of possible values for α assuming Hertz–Mindlin contact between spheres composed of a stable elastic material. DEM data points are from Specimen 3 with unrestrained particle rotation. Also shown are the theoretical curves given by Eqs. (10) (Voigt), (13) (Reuss: SC), (15) and (16) (self-consistent: BCC and SC, respectively), with $\xi = 0.55$ and $\xi = 1$. Also shown is an experimental data point for glass beads, for which the value of $\alpha \approx 0.9$ is uncertain because it assumes no inter-particle slip. A range of experimentally measured values of Poisson's ratio for quartz sand is also shown, for which the value of $\alpha \approx 0.8$ is uncertain for the same reason.

the specimens, shows that rotational mechanisms were present during the simulations. There appears, however, to be no correlation between $\langle \Omega \rangle_{\max} / \langle \Omega \rangle_{\text{avg}}$ and the internal parameter ξ for our DEM specimens.

5. Discussion

If we assume Hertz–Mindlin contact, then Eq. (8) of Part I implies that $\alpha = 2(1-\nu)/(2-\nu)$, where $\alpha = K_t/K_n$ and ν is Poisson's ratio for the material constituting the spheres (not for the particulate material as a whole). Thus, for a particulate material composed of uniform spheres, if the spheres are composed of a stable elastic material then α is bounded by $2/3 \le \alpha \le 4/3$, and if the spheres are composed of a stable elastic material with $0 \le \nu \le 1/2$ then α is bounded by $2/3 \le \alpha \le 1$. For materials with $\nu \approx 0.3$ (such as quartz), Hertz–Mindlin contact implies that $\alpha \approx 0.8$. Thus, the accuracy of theoretical models for values of α in the vicinity of 0.8, and more generally for values of α between 2/3 and 1, is of great practical importance. Fig. 10 shows the $\overline{\nu}(\alpha)$ curve for Specimen 3 in the region $2/3 \le \alpha \le 4/3$ with unrestrained particle rotation, along with the theoretical curves given by the Voigt (10), Reuss (13), and self-consistent (15) and (16) equations, with $\xi = 0.55$ and $\xi = 1$.

Also shown in Fig. 10 for comparison is an experimental data point for spherical glass beads. For glass beads, $\nu \approx 0.2$, and Hertz-Mindlin contact theory predicts $\alpha \approx 0.9$. Thus, the Voigt (10), Reuss (13), and self-consistent (15), (16) equations with $\xi = 1$, which also correspond to the equations of Section 3 in Part I derived assuming no particle rotation, all predict that Poisson's ratio for an isotropic packing of spherical glass beads should be $\overline{\nu} \approx 0.02$. However, according to Bachrach et al. (2000), the experimentally measured value of Poisson's ratio for a random packing of spherical glass beads is $\overline{\nu} \approx 0.15$, over seven times larger than the theoretical predictions of Section 3 in Part I. Note from Fig. 10, however, that the values of $\overline{\nu}$ predicted by the Voigt (10), Reuss (13), and self-consistent (15), (16) equations of Section 3 with $\xi = 0.55$ are much closer to the experimentally measured value of $\overline{\nu}$, ranging between $\overline{\nu} \approx 0.11$ and $\overline{\nu} \approx 0.14$ for $\alpha \approx 0.9$. It should be noted that the value of the internal parameter $\xi = 0.55$ was chosen to match the DEM data points obtained from Specimen 3, and by adjusting the internal parameter ξ any of the modified curves could be made to pass through the single experimental data point for glass beads. Specimen 3 was chosen in Fig. 10 for illustrative purposes, because it shows the largest effect of particle rotation of the six DEM specimens tested, and because the values of Poisson's ratio in the vicinity of $\alpha \approx 0.9$ are the closest to that measured experimentally for spherical glass beads.

Unfortunately, although it is illustrative, the experimental data point for glass beads provides limited information for the purpose of testing our theory. This is because, as noted by Bachrach et al. (2000), we do not know whether or not there was inter-particle slip between the glass beads during the experiment, and hence we do not know whether the value of $\alpha \approx 0.9$ predicted by Hertz–Mindlin contact theory (assuming no inter-particle slip) is correct for the glass beads. The same is true of the experimentally measured values of Poisson's ratio for quartz sand, which typically fall in the range $0.1 < \overline{\nu} < 0.2$ (e.g., Mitchell and Soga, 2005). This is one reason that the discrete element method was essential to test the validity of our theoretical results, since the value of α for any given physical particulate material (such as glass beads) is not known exactly, and at best provides only one data point, while using DEM we could adjust α over a large range of exactly known values by adjusting the inter-particle tangential contact stiffness K_t. Nevertheless, we note from Fig. 10 that the range of experimentally measured values of Poisson's ratio for quartz sand with $\alpha \approx 0.8$ compares well with our DEM simulation results obtained from Specimen 3.

Bachrach et al. (2000) noted the discrepancy between the experimentally measured value of $\overline{\nu}$ for a random packing of glass beads and the theoretical prediction of Walton (1987), which is identical to Eq. (10) with $\xi = 1$. Bachrach et al. (2000) suggested that the cause for this discrepancy may be due to slipping at the inter-particle contacts. A similar approach was taken by Trentadue (2004), who replaced the Hertz–Mindlin contact law in Eq. (8) of Part I with a Hertz–Cattaneo–Mindlin

contact law, which includes a parameter ζ to account for micro-slip at inter-particle contacts, and by Duffaut et al. (2010), who also modified the results of Walton (1987) by introducing a parameter to account for micro-slip at inter-particle contacts. While slipping at inter-particle contacts may be partially responsible for the very large discrepancy between the experimentally measured value of $\overline{\nu} \approx 0.15$ for a random packing of glass beads and the values predicted by the methods of Section 3 in Part I (with no particle rotation), slipping at inter-particle contacts cannot explain the discrepancy between the values of $\overline{\nu}$ that were measured from our DEM simulations and the values predicted by the methods of Section 3 in Part I, since we can verify that no slipping occurred between any of the particles in our DEM simulations. Indeed, by using DEM simulations to explore the effect of eliminating particle rotation, we believe that we have identified an important contributing factor to the discrepancy between theoretical and experimentally measured values of Poisson's ratio in particulate materials, particularly in the vicinity of $\alpha \approx 1$.

Another approach to the homogenization of particulate materials was taken by Cambou et al. (1995). Like Walton (1987) and Chang et al. (1995), Cambou et al. (1995) did not analyze specific local particle arrangements, but instead assumed a form for the distribution of inter-particle contact forces a priori. However, in addition to rederiving Eq. (24) of Part I or Eq. (10) with $\xi = 1$ under the Voigt hypothesis, Cambou et al. (1995) introduced an internal parameter μ in their "static localization method" (analogous to homogenization under the Reuss hypothesis) that measures the fraction of the deviatoric stress in the particulate material supported by the normal components of the inter-particle contact forces, from 2/5 for $\mu = 1$ to 1 for $\mu = 0$. Specifically, they assumed the average distribution f_i of the inter-particle contact forces at the local level within a particulate material can be expressed as a function of the orientation direction n_i and the far field (non-local) stress σ_{ij} as

$$f_i = \mu \sigma_{ij} n_j + \frac{1-\mu}{2}[5 n_j \sigma_{jk} n_k - \sigma_{jj}] n_i. \tag{17}$$

Eq. (17) was first proposed by Delyon et al. (1990), and it is based on the representation theorems (e.g., Spencer, 1987) under the assumptions that f_i is linear with respect to σ_{ij} and isotropic with respect to n_i. Static equilibrium then requires that

$$\sigma_{ij} = \beta D \int_{\Omega} f_i n_j \, d\Omega, \tag{18}$$

where $d\Omega = \sin\theta \, d\varphi \, d\theta \, d\psi$ is the differential solid angle of the unit sphere Ω, σ_{ij} is the far field stress in the particulate material, β is the average number of contacts per unit volume, and D is the diameter of the spheres. Under the hypotheses expressed in Eqs. (17) and (18), the relationship obtained by Cambou et al. (1995) between Poisson's ratio $\overline{\nu}$ and $\alpha = K_t/K_n$ by their static localization method is

$$\overline{\nu} = \frac{2\mu^2 + \alpha(5 - 10\mu + 3\mu^2)}{4\mu^2 + \alpha(20 - 20\mu + 6\mu^2)}. \tag{19}$$

Emeriault and Cambou (1996) derive more complicated expressions for an arbitrary anisotropic particulate material. If $\mu = 1$, then Eq. (19) is identical to Eq. (13) with $\xi = 1$, which is the same as the relation obtained by Chang et al. (1995) under their static hypothesis. Note that if $\mu = 0$, then none of the deviatoric stress in the particulate material is carried by the tangential components of the inter-particle contact forces. Thus, the role of μ in the analysis of Cambou et al. is similar to the role of ξ in our analysis. For $\mu < 1$, Eq. (19) does in fact predict a value of Poisson's ratio that is strictly greater than zero when $\alpha = 1.0$, which is in general agreement with what we have observed in our DEM simulations. However, as Fig. 11 shows, for no value of μ can the $\overline{\nu}(\alpha)$ curve given by Eq. (19) be made to match the curve obtained from our DEM simulations as closely as the curve given by Eq. (15).

While the internal parameter ξ cannot depend exclusively on the average number of contacts per unit volume β for reasons discussed in Section 3, we note that for the six DEM specimens described in the preceding section, there is, in fact,

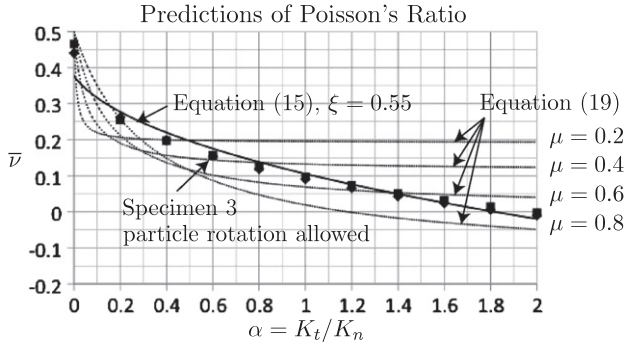

Fig. 11. The relationship between Poisson's ratio $\overline{\nu}$ and $\alpha = K_t/K_n$ as obtained by Cambou et al. (1995) by their static localization method, given by Eq. (19), for a range of values of their internal parameter μ. Also shown are the DEM data points from Specimen 3 with unrestrained particle rotation, and the curve given by the self-consistent equation (15) with $\xi = 0.55$.

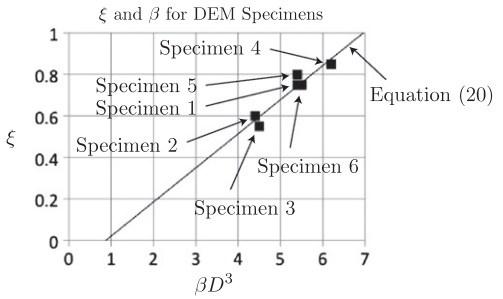

Fig. 12. Correlation between the internal parameter ξ and the average number of contacts per unit volume β for the six DEM specimens tested in Section 4, where D is the diameter of the spheres.

a strong correlation between ξ and β. Fig. 12 illustrates this correlation. It is noteworthy that the correlation between ξ and β observed in the DEM specimens appears to be independent of the number of spheres in the specimens (i.e., 3430 or 29 660). This suggests that the particle rotation effects observed in the DEM simulations described in Section 4 are not simply due to boundary effects, nor to the fact that the specimens are too small to represent a statistically isotropic particulate material. The best-fit line to the data points in Fig. 12 is given by

$$\xi = 0.164\beta D^3 - 0.143, \tag{20}$$

with an R^2 value of 0.905.

6. Conclusions

Building on the work of Part I, we have explored the effects of particle rotation on the elastic moduli of a statistically isotropic particulate material with locally cubic packing structure. We found that particle rotation effects *must* be properly accounted for to accurately predict the values of Poisson's ratio that were measured by our DEM simulations on six randomly packed specimens of uniform spheres, having constant normal and tangential contact stiffnesses K_n and K_t, respectively.

There were several advantages to using DEM to test our theoretical results, as opposed to, for example, using experiments on physical particles such as glass beads. First, we were able to reproduce our theoretical assumption of constant contact stiffness exactly, without having to make any assumptions regarding the actual contact behavior of the physical particles, thus eliminating one source of uncertainty. We were also able to assign precise values to the normal and tangential contact stiffnesses, and thus measure Poisson's ratio for a large range of specific values of $\alpha = K_t/K_n$. Finally, we were able to adjust the DEM simulations to either allow or prohibit particle rotation, and in this way study the effect of particle rotation on the values of Poisson's ratio. Specifically, we were able to prove that particle rotation was responsible for the values of Poisson's ratio predicted by the DEM simulations in the vicinity of $\alpha = 1$ being significantly higher than the theoretical predictions of Walton (1987) and Chang et al. (1995), which do not account for the mechanisms (i.e., zero-energy deformations) produced by particle rotation. In particular, the results of Chang et al. (1995) under the static hypothesis *do not* provide an upper bound on Poisson's ratio if particle rotation is allowed. This is despite the fact that Chang et al. (1995) attempted to include the effects of particle rotation via a "quasi-micro-polar" continuum theory. The inability of their approach to match the DEM simulation results appears to be due to the fact that the micro-polar or quasi-micro-polar continuum approach cannot capture the zero-energy strains or mechanisms produced by particle rotations, which we have shown can and do exist in random assemblies of uniform spheres where there are local asymmetries in the distribution of inter-particle contacts.

We also showed that this discrepancy between the theoretical and DEM predictions of Poisson's ratio could not be caused by inter-particle slip, since no inter-particle slip took place in our DEM simulations. This is a significant observation, since Bachrach et al. (2000) have hypothesized that inter-particle slip could be the cause for the (same) discrepancy between the theoretical prediction of Poisson's ratio by Walton and the experimentally measured value of Poisson's ratio for a random packing of uniform glass beads with $\alpha \approx 0.9$. While inter-particle slip may have taken place and contributed to the discrepancy, it cannot serve as the sole explanation, since the discrepancy still exists when no inter-particle slip takes place. It might also be noted that the results of such a comparison with experiment are difficult to interpret, since the theoretical value of Poisson's ratio depends on α, and α depends on the contact model assumed, which may itself be imperfect for the glass beads.

Based on a micromechanics analysis of the effect of particle rotation and the effect of the mechanisms caused by particle rotation in each of the three cubic elementary cells (FCC, BCC, and SC), we showed how our theoretical results could be modified by the introduction of an internal parameter ξ, which gave rise to an effective tangential stiffness $K_t^* = \xi K_t$, and hence an effective $\alpha^* = \xi\alpha$, where $0 \le \xi \le 1$ is a measure of the presence of shearing mechanisms due to particle rotation induced by local asymmetries in the distribution of inter-particle contacts. If $\xi = 0$ then all inter-particle contacts contain shearing mechanisms, and $\alpha^* = 0$. If $\xi = 1$ then there are no shearing mechanisms, and $\alpha^* = \alpha$. With this modification, our theoretical

results obtained under the self-consistent homogenization assumption, particularly that based on the body-centered cubic local packing geometry, are capable of providing remarkably good agreement with the results we obtained from our DEM simulations, especially when compared to the best theoretical estimates currently in the published literature.

Appendix A. Stiffness analysis of an FCC elementary cell with unrestrained particle rotation

In this appendix, we consider the stiffness of a single FCC elementary cell with unrestrained particle rotation subjected to a state of pure uniaxial compression along one of its principal axes: $-\delta_{11}$, $\delta_{22}=\delta_{33}=0$. In Section 2.1, we reported that an analysis of the inter-particle normal and tangential contact forces within a single FCC cell with *no particle rotation* for this state of deformation gives $F_{11}=-2(K_n+K_t)\delta_{11}$ and $F_{22}=F_{33}=-(K_n-K_t)\delta_{11}$ for the forces normal to the cell faces, and we noted that the normal and tangential stiffnesses of the contacts on the cell faces must contribute only half of their full values if the FCC cell is considered to be a constitutive material element of a larger material array. We also note, however, that if a single FCC cell is considered alone, then all of the contact forces must be included with their full values, and the measured forces normal to the cell faces will actually be $F_{11}=-3(K_n+K_t)\delta_{11}$ and $F_{22}=F_{33}=-(3/2)(K_n-K_t)\delta_{11}$. This is verified by DEM simulations.

If a single FCC elementary cell in which particle rotation is *unrestrained* is subjected to the state of pure uniaxial compression described in the last paragraph, then due to the symmetry of the loading only the spheres at the eight corners of the cell will experience rotation, and we can simplify our analysis by considering only the four spheres in contact at one corner of the FCC cell where only the corner sphere has rotational degrees of freedom. Fig. A1 shows the four spheres that we will analyze. These four spheres are in the configuration of a tetrahedron. For the state of pure uniaxial compression in the $\hat{e}_1$ direction: $-\delta_{11}$, $\delta_{22}=\delta_{33}=0$, Spheres 1 and 4 in Fig. A1 experience a displacement of $-\delta_{11}/2$ in the $\hat{e}_1$ direction, and Spheres 2 and 3 remain fixed. If we denote the force contribution in the $\hat{e}_i$ direction from the contact between Spheres a and b as $(f_{ab})_{ii}$ (no sum), then we have

$$(f_{12})_{11}=(f_{13})_{11}=-(1/4)(K_n+K_t)\delta_{11}, \tag{A.1}$$

$$(f_{12})_{22}=(f_{13})_{33}=-(1/4)(K_n-K_t)\delta_{11}, \tag{A.2}$$

$$(f_{12})_{33}=(f_{13})_{22}=0. \tag{A.3}$$

Because Spheres 2 and 3 remain fixed, we have

$$(f_{23})_{11}=(f_{23})_{22}=(f_{23})_{33}=0. \tag{A.4}$$

If Sphere 4 has rotational degrees of freedom $\delta\theta_1$, $\delta\theta_2$, and $\delta\theta_3$ about the principal axes $\hat{e}_1$, $\hat{e}_2$, and $\hat{e}_3$, respectively, then for small rotations we have

$$(f_{24})_{11}=-(1/4)(K_n+K_t)\delta_{11}-R\delta\theta_2K_t/\sqrt{2}, \tag{A.5}$$

$$(f_{24})_{22}=0, \tag{A.6}$$

$$(f_{24})_{33}=-(1/4)(K_n-K_t)\delta_{11}+R\delta\theta_2K_t/\sqrt{2}, \tag{A.7}$$

$$(f_{34})_{11}=-(1/4)(K_n+K_t)\delta_{11}+R\delta\theta_3K_t/\sqrt{2}, \tag{A.8}$$

$$(f_{34})_{22}=-(1/4)(K_n-K_t)\delta_{11}-R\delta\theta_3K_t/\sqrt{2}, \tag{A.9}$$

$$(f_{34})_{33}=0, \tag{A.10}$$

where R is the radius of the spheres. By symmetry, it is clear that $\delta\theta_1=0$. While the rotational degrees of freedom $\delta\theta_2$ and $\delta\theta_3$ do result in a relative tangential displacement at the point of contact between Spheres 1 and 4, this displacement results in equal and opposite contributions to the total force in the $\hat{e}_1$ direction, and so we have

$$(f_{14})_{11}=(f_{14})_{22}=(f_{14})_{33}=0. \tag{A.11}$$

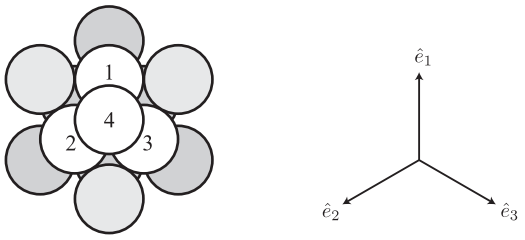

Fig. A1. The four numbered spheres that we analyze, which are in the configuration of a tetrahedron, and the principal directions for a single FCC elementary cell.

Moment equilibrium for Sphere 4 requires that $R\delta\theta_2 = -R\delta\theta_3 = -\delta_{11}/(5\sqrt{2})$. Thus, it follows that

$$(f_{24})_{11} = (f_{34})_{11} = -(1/4)(K_n + (3/5)K_t)\delta_{11}, \tag{A.12}$$

$$(f_{24})_{33} = (f_{34})_{22} = -(1/4)(K_n - (3/5)K_t)\delta_{11}. \tag{A.13}$$

Due to the symmetry of the FCC elementary cell, the total forces in the principal directions $\hat{e}_1$, $\hat{e}_2$, and $\hat{e}_3$ normal to cell faces are

$$F_{11} = 2(f_{12})_{11} + 2(f_{13})_{11} + 4(f_{24})_{11} + 4(f_{34})_{11}, \tag{A.14}$$

$$F_{22} = 2(f_{12})_{22} + 2(f_{23})_{22} + 4(f_{24})_{22} + 4(f_{34})_{22}, \tag{A.15}$$

$$F_{33} = 2(f_{13})_{33} + 2(f_{23})_{33} + 4(f_{24})_{33} + 4(f_{34})_{33}. \tag{A.16}$$

From Eqs. (A.14)-(A.16), it follows that $F_{11} = -3(K_n + \xi K_t)\delta_{11}$ and $F_{22} = F_{33} = -(3/2)(K_n - \xi K_t)\delta_{11}$, with $\xi = 11/15 \approx 0.733$. This is the value of ξ reported in Section 2.1.

Note that the value of $\xi = 11/15 \approx 0.733$ is only valid when the FCC elementary cell is considered alone. If the FCC cell is considered to be a constitutive material element of a larger material array, then the stiffnesses of the inter-particle contacts on the faces of the cell should contribute only half of their full values, as described for the case of no particle rotation at the beginning of this appendix. For the case of unrestrained particle rotation, this leads to $F_{11} = -2(K_n + \xi K_t)\delta_{11}$ and $F_{22} = F_{33} = -(K_n - \xi K_t)\delta_{11}$, with $\xi = 4/5 = 0.8$.

The DEM simulations described in Section 2.1 performed on a single FCC elementary cell were performed on a single FCC cell in which the inter-particle contact stiffnesses at all contact points were the same. Thus, the value of $\xi = 11/15 \approx 0.733$ and not the value of $\xi = 4/5 = 0.8$ was observed in the DEM measurement of Poisson's ratio for a single FCC elementary cell in Section 2.1, which is shown in Fig. 2. We also saw in Section 2.1 that when an FCC elementary cell becomes a part of a larger FCC array, particle rotation becomes *partially restrained*, and this leads immediately to $\xi > 0.8$ (even for a $2 \times 2 \times 2$ array). Thus, for consistency of presentation, we reported $F_{11} = -2(K_n + \xi K_t)\delta_{11}$ and $F_{22} = F_{33} = -(K_n - \xi K_t)\delta_{11}$, with $\xi = 11/15 \approx 0.733$ in Section 2.1 for a single FCC elementary cell with unrestrained particle rotation subjected to a state of pure uniaxial strain in the $\hat{e}_1$ direction, in analogy to the case of no particle rotation where the FCC elementary cell is considered to be a constitutive material element of a larger material array.

References

Bachrach, R., Dvorkin, J., Nur, A.M., 2000. Seismic velocities and Poisson's ratio of shallow unconsolidated sands. Geophysics 65, 559–564.

Bardet, J.P., Vardoulakis, I., 2001. The asymmetry of stress in granular media. Int. J. Solids Struct. 38, 353–367.

Cambou, B., Dubujet, P., Emeriault, F., Sidoroff, F., 1995. Homogenization for granular materials. Eur. J. Mech. A/solids 14, 225–276.

Chang, C.S., Chao, S.J., Chang, Y., 1995. Estimates of elastic moduli for granular material with anisotropic random packing structure. Int. J. Solids Struct. 32, 1989–2008.

Chang, C.S., Gao, J., 1995. Second-gradient constitutive theory for granular material with random packing structure. Int. J. Solids Struct. 32, 2279–2293.

Chang, C.S., Liao, C.L., 1990. Constitutive relations for particulate medium with the effect of particle rotation. Int. J. Solids Struct. 26, 437–453.

Cundall, P.A., Strack, O.D.L., 1979. A discrete numerical model for granular assemblies. Géotechnique 29, 47–65.

Delyon, F., Dufresne, D., Levy, Y., 1990. Physique et genie civil: deux illustrations simples. Mecanique des milieux granulaires. Annales des Ponts et Chaussees numero special, 53–60.

Duffaut, K., Landrø, M., Sollie, R., 2010. Using Mindlin theory to model friction-dependent shear modulus in granular media. Geophysics 75, E143–E152.

Durán, O., Kruyt, N.P., Luding, S., 2010. Analysis of three-dimensional micro-mechanical strain formulations for granular materials: evaluation of accuracy. Int. J. Solids Struct. 47, 251–260.

Emeriault, F., Cambou, B., 1996. Micromechanical modelling of anisotropic non-linear elasticity of granular medium. Int. J. Solids Struct. 33, 2591–2607.

Fleischmann, J.A., Drugan, W.J., Plesha, M.E., 2013. Direct micromechanics derivation and DEM confirmation of the elastic moduli of isotropic particulate materials: Part I no particle rotation. J. Mech. Phys. Solids., 61, 1569–1584.

Goddard, J.D., 2008. From granular matter to generalized continuum. In: Capriz, G., Giovine, P., Mariano, P. (Eds.), Mathematical Models of Granular Matter. Springer. Lecture Notes in Mathematics, vol. 1937, pp. 1–22.

Hershey, A.V., 1954. The elasticity of an isotropic aggregate of anisotropic cubic crystals. J. Appl. Mech. 21, 236–240.

Jenkins, J., Johnson, D., La Ragione, L., Makse, H., 2005. Fluctuations and the effective moduli of an isotropic, random aggregate of identical, frictionless spheres. J. Mech. Phys. Solids 53, 197–225.

Jenkins, J.T., Cundall, P.A., Ishibashi, I., 1989. Micromechanical modeling of granular materials with the assistance of experiments and numerical simulations. In: Biarez, J., Gourvès, R. (Eds.), Powders and Grains. Balkema, Rotterdam, pp. 257–264.

Kröner, E., 1958. Berechnung der elastischen Konstanten des Vielkristalls aus den Konstanten des Einkristalls. Z. Phys. 151, 504–518.

Kruyt, N.P., 2003. Statics and kinematics of discrete Cosserat-type granular materials. Int. J. Solids Struct. 40, 511–534.

Mitchell, J.K., Soga, K., 2005. Fundamentals of Soil Behavior. John Wiley and Sons.

Nemat-Nasser, S., 2004. Plasticity: A Treatise on Finite Deformation of Heterogeneous Inelastic Materials. Cambridge University Press.

Oda, M., 1997. A micro-deformation model for dilatancy of granular materials. In: Chang, C., Misra, A., Liang, R., Babic, M. (Eds.), Mechanics of Deformation and Flow of Particulate Materials. ASCE, pp. 24–37.

Reuss, A., 1929. Calculation of flow limits of mixed crystals on the basis of the plasticity of single crystals. Z Angew. Math Mech 9, 49.

Spencer, A.J.M., 1987. Isotropic polynomial invariants and tensor functions. In: Boehler, J. (Ed.), Applications of Tensor Functions in Solid Mechanics. Springer.

Suiker, A.S.J., de Borst, R., 2005. Enhanced continua and discrete lattices for modelling granular assemblies. Philos. Trans. R. Soc. A 363, 2543–2580.

Trentadue, F., 2004. An equilibrium-based approach for the micromechanical modelling of a non-linear elastic granular material. Mech. Mater. 36, 323–334.

Voigt, W., 1928. Lehrbuch der Kristallphysik. Teubner, Leipsig, Germany.

Walton, K., 1987. The effective elastic moduli of a random pack of spheres. J. Mech. Phys. Solids 35, 213–226.